Master`s Thesis

LIQUID SURFACE DEFORMATION

NEAR METAL SURFACE

Myung-Won Song

Department of Physics

Graduate School of UNIST

2018

1

LIQUID SURFACE DEFORMATION

NEAR METAL SURFACE

Myung-Won Song

Department of Physics
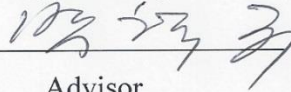
Graduate School of UNIST

Liquid Surface Deformation Near metal surface

A thesis/dissertation
submitted to the Graduate School of UNIST
in partial fulfillment of the
requirements for the degree of
Master of Science

Myung-won Song

06/15/2018 of submission

Approved by
_____
Advisor
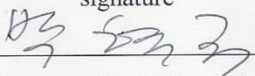Hyuk-Kyu Pak

Liquid Surface Deformation Near Metal Surface

Myung-Won Song

This certifies that the thesis/dissertation of Myung-won Song
is approved.
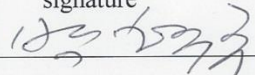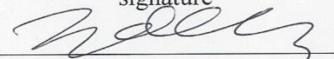
06/15/2018 of submission

signature

_____
Advisor: Hyuk Kyu Pak

signature

_____
Hyuk Kyu Pak: Thesis Committee Member #1

signature

_____
Yongseok Jho: Thesis Committee Member #2

signature

_____
Joonwoo Jeong: Thesis Committee Member #3

Abstract

A solid surface in contact with water or aqueous solution carries specific electric charges. We observed voltage generation during the initial contact and spreading of a water droplet on solid surface. Simultaneously, high speed camera was used to study the water droplet spreading phenomena. After the initial contact, a water droplet spreads for 6 ms. The spreading radius on the solid surface follows a well-defined power-law dynamic. During this short time region (<6ms), monotonic increase of voltage generation was observed as well. In this study, correlation between water droplet spreading and voltage generation is studied by using the electric double layer capacitor (EDLC) model.

We studied water droplet surface deformation by using interferometric method, RICM(Reflection Interference Contrast Microscope) is measurement of the interference fringe pattern between light reflected from ITO electrode and it reflected from the water droplet surface. While, water droplet is approaching to the ITO electrode, interference fringe pattern change was remarkably deviated from the theoretical curve. Surprisingly, deviation of curve from the theoretical curve is starting from ~300nm far from the ITO electrode, and measured deformation amount of water surface was ~100nm. Based on the radius dependence of deformation amount, surface morphology change due to the distance change was accomplished.

For the further analysis of correlation between water droplet spreading and electric signal, we used the interferometric technique which gives the information about the shape change of the droplet during the spreading. This method can measure both the water droplet spreading and electrical properties on the solid-liquid interfaces at the same time and will be useful in the study of electrical phenomena on solid–liquid interfaces.

Contents

List of Figure

List of Tables

Explanation of terms and abbreviations

EDL	Electrical Double Layer
EDLC	Electrical Double Layer Capacitor
SFA	Surface Force Apparatus
RICM	Reflection Interference Contrast Microscope
ITO	Indium Tin Oxide
IHP	Inner Helmholtz Plane
OHP	Outer Helmholtz Plane
RT	Room Temperature
RH	Relative Humidity

1. Introduction

Solid-liquid interfaces are everywhere around us, such as energy storage systems[1-2], biological and medical systems[3-4], water filtering systems[5-6], and electronics7[-8]. In spite of tremendous studies, understanding the solid-liquid interface is still challenging due to the lack of efficient experimental techniques. Biggest difficulty is the charge screening at the interfaces. Most objects in contact with water or an aqueous solution acquire some electronic charges on their surfaces. Therefore, the charges in the liquid side feel the surface potential of the solid surface due to Coulomb interaction. The surrounding dielectric molecules in liquid decrease the magnitude of the Coulomb interaction[2,9-10]. Additionally, the charges on the surface attract the counter ions from the liquid side, which electrically screen the surface charges. This charge screening allows only the short-range distribution of interfacial charges, called as the electric double layer (EDL). Since the penetration of electric field is limited due to the small charge screening length, EDLs of solid-liquid interfaces are remained as the big challenges.

To investigate the EDL, numerous techniques have been used, such as X-ray reflectivities[11-12], Surface-Force Apparatus (SFA)[13-14], non-linear optics[15-16], electrical experiments[17-19], and theoretical simulations [9,10,20]. Among them, direct measurement techniques of force are SFA or Atomic Force Microscopy (AFM).
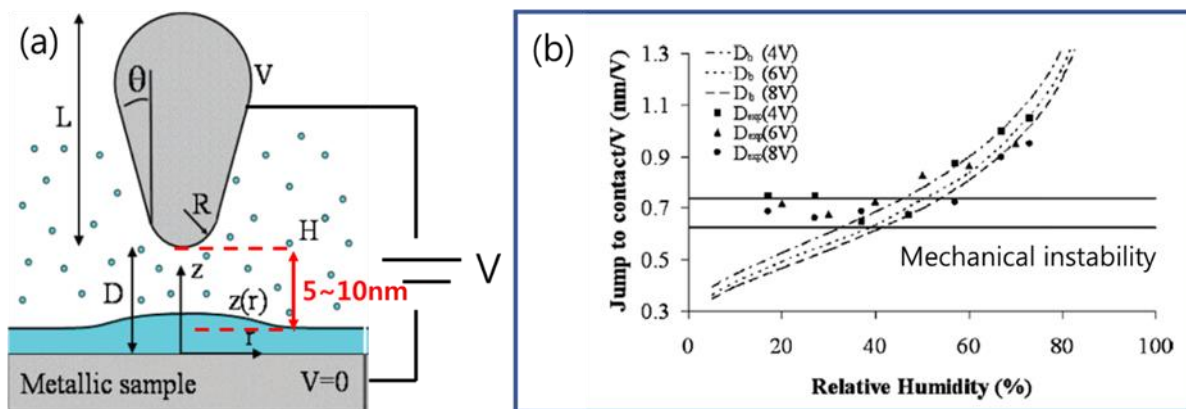
Figure 1-1 (a) Geometry of the system with tip and water film layer. It measures the formation of a water bridge under high humidity and externally applied voltage applied to the tip. (b) Jump-

to-contact distance (water bridge size) normalized to the bias voltage as a function of relative humidity condition. [21]

Sacha et. al. observed a water bridge formation between an AFM tip and a water film layer with external applied electric field by approaching the AFM tip with nano-meter resolution as shown in Figure 1-1.[21-22] They argued that the origin of water formation is mixed effect of condensation and Coulomb interaction.

$$U_{total} = U_{electro\ static} + U_{condensation} \quad (1.1)$$

Here, $U_{electro\ static}$ is the electrostatic energy related to the applied voltage and $U_{condensation}$ is the capillary condensation energy. This observation is effect from the externally applied electric field. It is a lot different from our work in which there is no externally applied electric field.
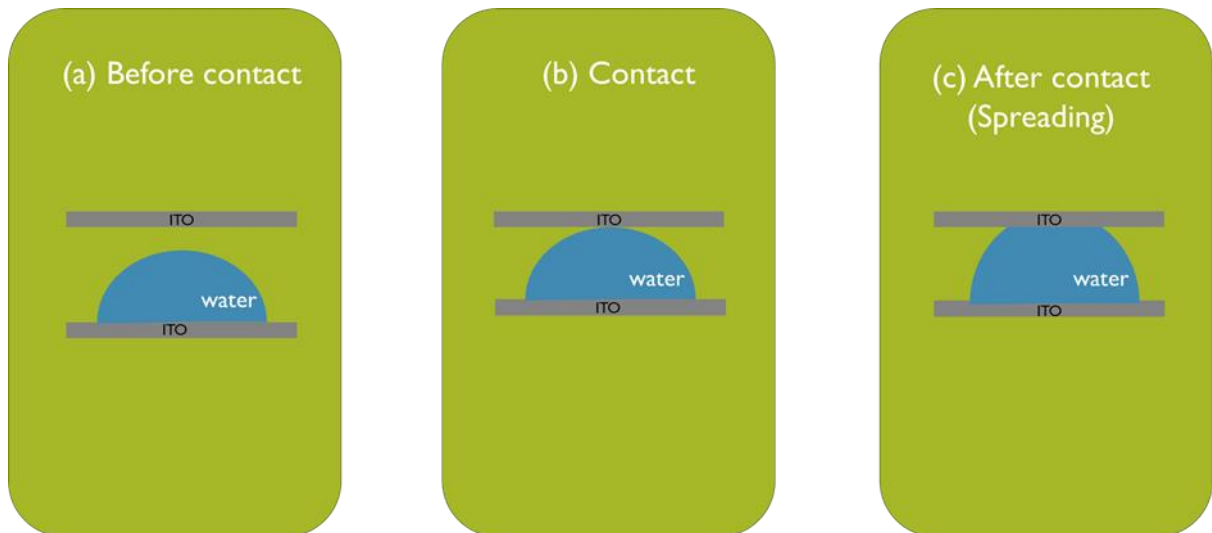
Figure 1-2. Contact process of water droplet and solid substrate (a) Before contact, the droplet sits on the bottom substrate and is in electrical equilibrium. (b) At the moment of contact, the surface of water droplet deforms. (c) After contact, the droplet spreads on top substrate

Figure 1-2 shows the contact process when liquid droplet close slowly to solid surface. The contact process can be divided into three stages: (a) before contact, (b) just before and at the moment of contact, and (c) spreading after contact. In this study, we build up a homemade experimental system: combination of a Reflection Interference Contrast Microscopy (RICM) and voltage generation system. RICM is an optical measurement technique with very high distance resolution by using the interference pattern along the surface normal direction. It has been applied also to study the spreading dynamics[23-24] and the evaporation of water droplet[25]. In this study, the RICM is used to study quantitatively the water bridge formation dynamics. Due to the induced charge distribution at the interface of liquid-solid

interface, during the contacting process, the electrical potential difference between two substrates changes with time. The voltage generation system measures this potential difference to characterize the process. Since we are interested in the study of solid-liquid interface at natural condition, no external voltage is applied to both liquid drop and solid substrate in our study.

Chapter II explains the theory of droplet spreading on solid surface, the electrical double layer, and the principles of voltage generation and RICM. Chapter III describes the experimental procedures. As water droplet is linearly approached with time to the ITO electrode, interference fringe patterns from RICM describe the surface morphology of the water droplet. Simultaneous voltage measurements describe the electrical potential information on two liquid-solid interfaces. Chapter IV shows the experimental results and suggests the possible origin of the observations. The correlation between the spreading dynamics and voltage generation are also studied.

2. Theory

2.1 Liquid droplet spreading dynamics

Spreading of liquid on any surface, unless the surface is super-hydrophobic, is a common phenomenon observed in our everyday lives. Liquid spreads immediately after brought into contact with a substrate. The dynamics of spreading is an important question in many other applications such as printing, coating, pharmaceutical, etc.

The growth dynamics of spreading radius follows the power law of $r \sim t^{\alpha}$. The growth exponent α changes its value depending on its stage during the spreading process. At the last stage of spreading, the drop approaches its final equilibrium shape and the radius of the wetted area grows with $r \sim t^{1/10}$.[26] This dynamics can be explained by the competition between capillary force from the curvature at the contact point and viscous forces. These forces become weaker as the radius increases, which limits infinite spreading of liquid. Spreading is much faster at the early stage than at the later stage. However, the dynamics of spreading in the early stage is not much understood yet. The exponent α depends on the wetting properties of surface. For complete wetting surface such as low-viscosity liquid like water on glass surface, the radius of wetted area follows $r \sim t^{1/2}$.[26-28]
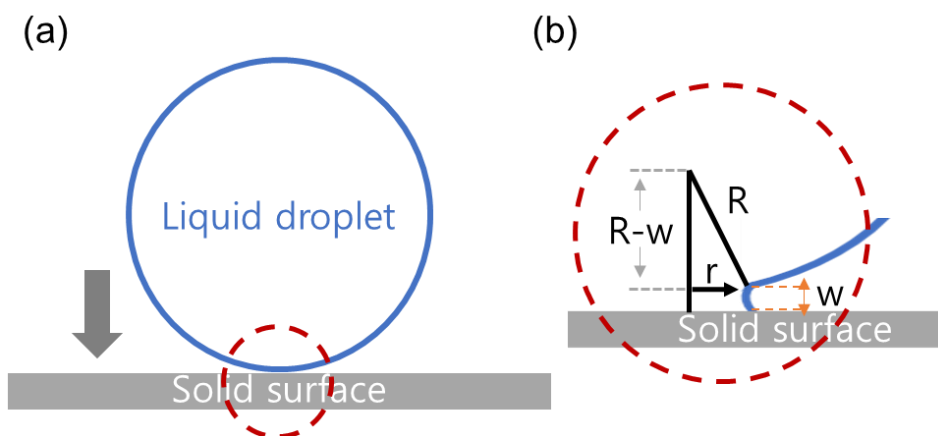
Figure 2-2 Geometry of a liquid droplet with initial radius R in the initial state of spreading. W is width of the narrow gap

When a liquid droplet contacts with a solid surface as shown in Figure 2-1, there are two radii (r and

w) involved as shown in (b). At the instant of contact, the curvature of the contact area is infinite, leading to a diverging Laplace pressure jump. This induces a rapid flow in the drop that replenishes the liquid neck, yielding a wetted area that grows in time. Since the r is the radius between the liquid and the substrate, it cannot drive the flow. Therefore, the capillary pressure (Laplace pressure) of the radius w is responsible for the flow. This pressure

$$\text{Capillary pressure} \quad \Delta P = \gamma \left(\frac{1}{r} - \frac{2}{w} \right) \qquad (2.1)$$

Using the relation between w and r we can calculate w at the early stage where w<<r

$$\Delta P \sim \frac{\gamma}{w} \qquad (2.2)$$

Using Figure 2-1(b), we can find relation R and w

$$(R - w)^2 + r^2 = R^2$$

$$w = R - \sqrt{R^2 - r^2}$$

$$= R - R\sqrt{1 - \left(\frac{r}{R}\right)^2}$$

$$= R - R\left(1 - \frac{1}{2}\left(\frac{r}{R}\right)^2 + \cdots\right) = \frac{1}{2}\frac{r^2}{R}$$

$$\therefore w = \frac{1}{2}\frac{r^2}{R} \qquad (2.3)$$

Balance of the inertial energy and capillary energy per volume.

$$\text{Inertial energy} \quad \rho v^2 = \rho \left(\frac{dr}{dt}\right)^2, \quad \text{Capillary energy} \quad \Delta P = \gamma \frac{R}{r^2}$$

$$\frac{\gamma}{w} = \rho v^2$$

$$= \rho \left(\frac{dr}{dt}\right)^2. \qquad (2.4)$$

γ/w is the energy per unit volume and becomes an inertial spreading energy per unit volume (kinetic energy per unit area) $\rho(dr/dt)^2$. [28-29] Here, ρ is the density of liquid, and γ is the surface tension. Therefore, in order to make a balance of the inertial and the capillary energy in the unit volume, we put Equation (2.3) into Equation (2.4).

$$\frac{dr}{dt} = \left(\frac{\gamma}{\rho w}\right)^{\frac{1}{2}}$$

$$= \frac{1}{r}\left(\frac{\gamma R}{\rho}\right)^{\frac{1}{2}}$$

$$\int r\, dr = \int \left(\frac{\gamma R}{\rho}\right)^{\frac{1}{2}} dt$$

$$\frac{1}{2}r^2 = \left(\frac{\gamma R}{\rho}\right)^{\frac{1}{2}} t$$

$$\therefore r \sim \left(\frac{\gamma R}{\rho}\right)^{\frac{1}{4}} t^{\frac{1}{2}} \tag{2.5}$$

Therefore, in the early stage, the spreading radius follows the relation $r \sim \left(\frac{\gamma R}{\rho}\right)^{\frac{1}{4}} t^{\frac{1}{2}}$ with the spreading exponent $\alpha = 1/2$.

$$\frac{r}{R} = A\left(\frac{t}{t_c}\right)^{\frac{1}{2}} \text{, where } t_c = \sqrt{\frac{\rho R^3}{\gamma}}$$

$$\therefore r \propto t^{\frac{1}{2}} \tag{2.6}$$

Here, t_c is the characteristic time of the inertial regime. For the water droplet with R=0.5 mm, this time is $t_c \sim 1.32$ ms.[24] Therefore, for low-viscosity liquid such as water, in inertial regime the spreading radius grows as $r \propto t^{\frac{1}{2}}$.
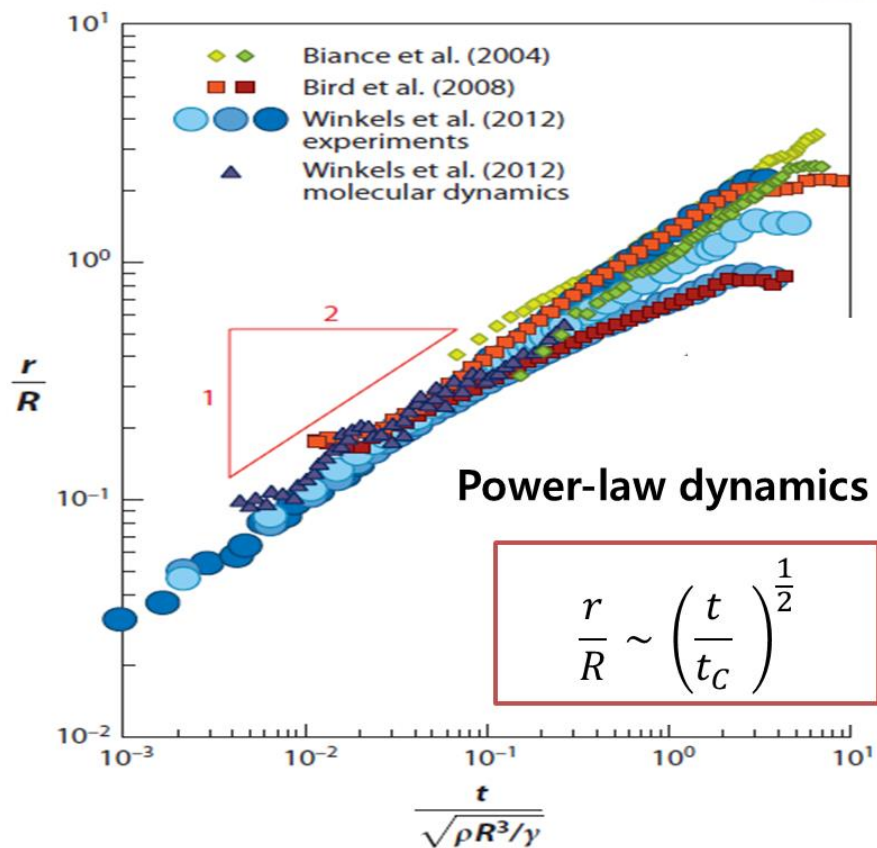
Figure 2-3 Spreading dynamics from four previous works. Here, the contact radius in the vertical axis and the time in the horizontal axis are normalized by the spherical drop radius and the characteristic inertial time, $t_c = \sqrt{\rho R^3/\gamma}$, respectively[29].

Figure 2-2 shows the data of the spreading dynamics from four different previous works. The spreading radius r is measured as a function of time t, on a log-log scale. All works show that the spreading exponent is $\frac{1}{2}$ in the early growth stage.[29]

2.2 Electrical double layer capacitor model

A solid surface in contact with water or aqueous solution usually carries specific electric charges. These surface charges attract counter ions from the liquid side. Since the geometry of opposite charge distribution in parallel at the solid-liquid interface is similar to that of a capacitor, it is called as an electrical double layer capacitor (EDLC).[18-19] Due to the opposite charge distribution, there is an electrical potential difference across the EDLC in equilibrium.[18-19]
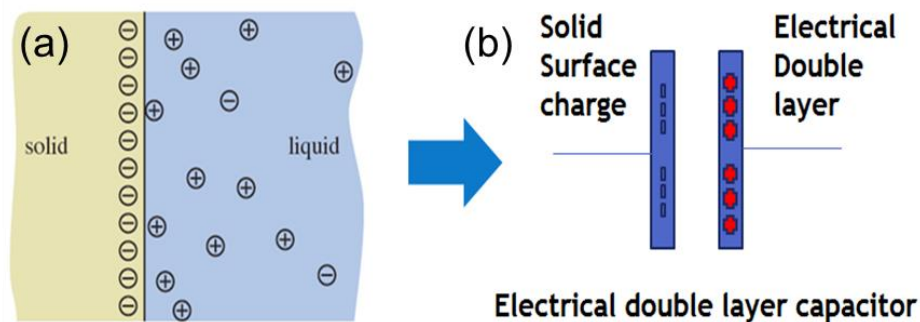
Figure 2-3 (a) Equilibrium distribution of charges when the solid is in contact with water or an aqueous solution. (b) This geometry and structure are similar to an electric capacitor.
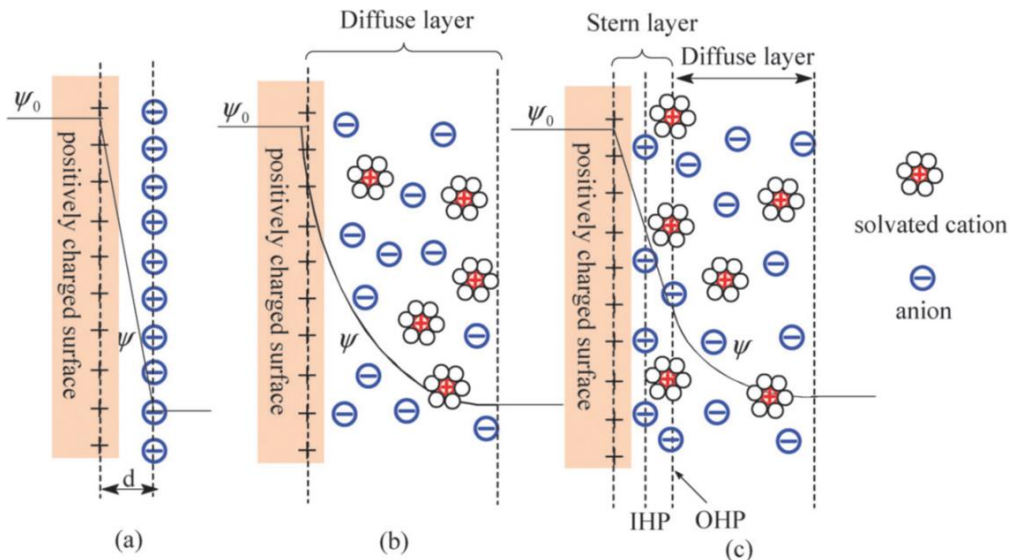
Figure 2-4. Three different electrical double layer (EDL) models: (a) Helmholtz model, (b) Gouy-Chapman model, and (c) Stern model. Ψ_0 is surface potential of solid, and Ψ is decay curve of surface potential. IHP and OHP mean Inner Helmholtz Plane and Outer Helmholtz Plane, respectively[2].

Figure 2-4 shows three different EDL models[2,36-38]. Helmholtz model in (a) is the simplest approximation that the surface charges are neutralized by counter ions placed at distance d from surface. Therefore, the surface charge potential decreases linearly from the surface to the counter ions satisfying the charge neutrality. The theoretical treatment of Helmholtz model does not adequately explain all the features, since it hypothesizes the rigid layer of opposite charges. Gouy-Chapman model in (b) explains the ion distribution due to thermal fluctuation. In this model, counter ions are considered as point charges forming diffuse double layer in which the change in concentration of the counter ions near a charged surface follows the Boltzmann distribution,

$$n = n_0 exp(-ze\Psi/kT). \qquad (2.7)$$

Here, n_0 is bulk concentration, z is charge on the ion, e is charge on a proton, k is Boltzmann constant, and T is temperature. Stern model in (c) explains the combination Helmholtz and Gouy-Chapman models. The first layer of solvated ions of finite size is tightly adsorbed onto the surface and the subsequent layers composed of point charges like in the Gouy-Chapman model. Therefore, at high surface charge potential, the diffuse layer between the surface and solution charge zones decrease toward zero and d increase.

2.3 Voltage generation during the water droplet spreading
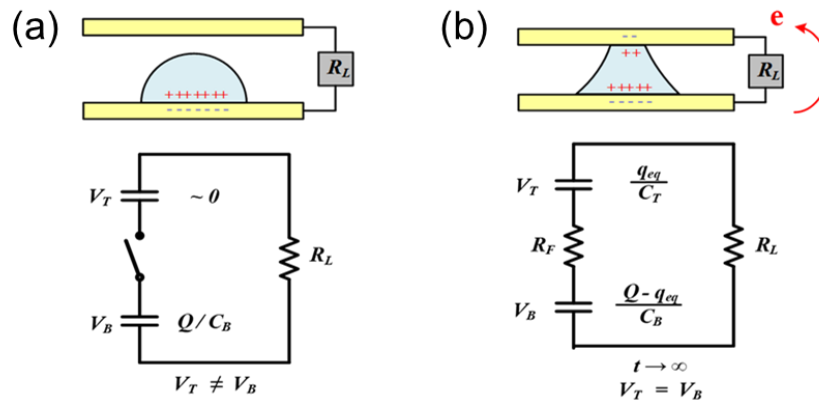
Figure 2-5. (a) Equilibrium charge distribution and its equivalent circuit model before the water bridge is formed. (b) Equilibrium charge distribution after the water bridge is formed and its equivalent circuit model[18-19].

When a water droplet is in contact with the top electrode, the solid-liquid interface forms an EDL as shown in Figure 2-5. Figure 2-5(a) shows the equilibrium charge distribution at the electrode-water interface before the water bridge is formed, with a water droplet just sitting on the bottom electrode. Due to the interaction between the mobile electrons of the electrode and the counter ions in water, the electrons and counter ions form a parallel dipole distribution at the interface of the bottom electrode. Figure 2-5(b) shows the equilibrium charge distribution at the electrode-water interfaces when a liquid bridge is formed between the droplet and the top electrode. As soon as the top electrode makes a contact with the water droplet sitting on the bottom electrode, electrons flow through the circuit (and load resister) to lower the free energy in the system. Due to the voltage difference between top and bottom electrodes, electrons flow from the bottom to the top and the counter ions in the water will be redistributed in the direction favoring an elimination of the voltage difference between the top and the bottom electrodes. The voltage difference between the two EDLCs becomes zero when an equilibrium condition is reached. In this state, the voltages of the system are given by Kirchhoff's law

$$\frac{Q-q(t)}{C_B} - \frac{q(t)}{C_T(t)} = 0, \ Q \gg q(t) > 0 \ and \ C_B \gg C_T(t) \qquad (2.8)$$

Here, Q is the initial charge in the bottom electrode, $q(t)$ is the increment (decrement) of charge in the top (bottom) after the closed circuit is formed, and C_B (C_T) is the capacitance of the bottom (top) interface. Contacting a water droplet with the top electrode is the same as closing the switch in the electric circuit. When the top electrode makes a contact with the water droplet, electrons flow from the bottom EDLC to the top EDLC through the load resistor and the counter ions in the water become redistributed.[18-19] Following equation describes this non-equilibrium behaviour.

$$\frac{Q-q(t)}{C_B} - \frac{q(t)}{C_T(t)} = \frac{dq}{dt} R_{tot} = V(t) \qquad (2.9)$$

Here, R_{tot} is the total resistance of the system. Since the capacitance of EDLC can be assumed as $C = \varepsilon_0 \varepsilon A/d$ and the bottom contact area is not changing is with time, the bottom EDLC C_B is constant. But the contact area of the top interface is changing during the bridge formation, therefore C_T is time dependent. Since the contact area of top electrode can be related with the radius of the top contact area, $A_T(t) = \pi (r(t))^2$, we can find the relation between the spreading radius $r(t)$ and the measured voltage $V(t)$. The increment of charge in the top after the closed circuit is formed can be calculated using the voltage measurement with time using the Ohm's law.

21

$$q(t) = \frac{1}{R_{tot}} \int V(t)dt, \tag{2.10}$$

The capacitance of top interface, $C_T(t)$, can be rewritten from Equation (2.9).

$$C_T(t) = \frac{C_B \cdot q(t)}{Q_B - q(t) - C_B V(t)}. \tag{2.11}$$

The capacitance of the top interface can be $C_T(t) = \frac{\varepsilon_T A_T(t)}{d_T}$, where d corresponds to the electrical double layer thickness at top interface. From Equation (2.11), we can obtain the relation between the spreading radius $r(t)$ and the measured voltage $V(t)$ as following.

$$\frac{\varepsilon_T \pi (r(t))^2}{d_T} = \frac{C_B \cdot q(t)}{Q_B - q(t) - C_B V(t)}, \tag{2.12}$$

$$r(t) = \left(\frac{d_T}{\varepsilon \pi} \cdot \frac{C_B \cdot q(t)}{Q_B - q(t) - C_B V(t)} \right)^{\frac{1}{2}}. \tag{2.13}$$

Here, ε_0, ε, $d_B(d_T)$ are dielectric constant of air, relative dielectric constant of medium, and electrical double layer thickness at bottom (top), respectively.

2.4 Reflection Interference Contrast Microscope (RICM)

Reflection interference contrast microscopy (RICM) is one of the optical microscopy techniques that utilize the interference property of light. Figure. 2-5 shows the simplified schematics showing the principle of RICM. A LED light is introduced to the sample surface through a flat ITO glass slide. Part of the light is reflected on the ITO glass surface and the rest is reflected on the sample surface.
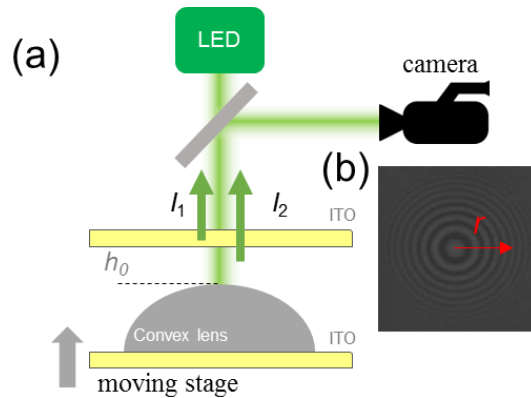
Figure 2-6 (a) Simplified schematics of RICM. Interference fringe pattern is due to two reflected beams, I_1 and I_2. Phase difference between two beams is determined by path length difference of $2h_0$. (b) Interference fringe pattern between plano-convex lens surface and top surface.

In this figure, in order to test the system, a plano-convex lens is placed on the bottom electrode and a beam splitter is used to observe the interference image using a camera. A light is illuminated from the side using a beam splitter. According to the distance from the surface of the convex lens to the top surface of the ITO glass slide, two reflected beams form an interference pattern due to the phase difference on the camera. As the position is radially away from the center of the convex lens, this distance increases and the light path also increases causing a change in the phase difference. As shown in (b) in Figure 2-6, depending on the path difference, a constructive interference and a destructive interference will occur alternately. Following shows the condition for each interference.

$$2\ell = (2m + 1)\frac{\lambda}{2} \quad \textbf{Constructive interference} \qquad (2.14)$$

$$2\ell = m\lambda \qquad \textbf{Destructive interference} \qquad (2.15)$$

Here, ℓ is the distance between the surface of the convex lens and the top surface of[the ITO glass slide and m is $0, \pm1, \pm2, \pm3$. Reflected beam intensity from the top ITO (I_1) is fixed. Actually, there are two reflected beams from the ITO: one from the upper surface and the other from the bottom surface of top ITO glass slide), but both do not depend on the sample height change (h_0). But, another reflected beam intensity from the plano-convex lens surface (I_2) depends on the sample height ($h(r=0) = h_0$). We neglected height dependency of I_1 in the following equation. But height dependency of I_1 is considered when we fit our data. The total reflected beam intensity (I) is function of the phase difference ($\emptyset$) from the path length difference between two reflected beams.[39-41]

$$I(h_0(r)) = I_1 + I_2 + 2\sqrt{I_1 I_2}\cos\emptyset(h_0(r)), \qquad (2.16)$$
$$\emptyset(h_0(r)) = 2k h_0(r) + \delta_0, \qquad (2.17)$$

Here, k and δ_0 are wavenumber of light in the air and initial phase difference between I_1 and I_2, respectively. $h_0 = 0$ is defined when a plano-convex lens contacts to the plane glass.

3. Method and experiment

3.1 Sample preparation

Pure deionized water with 18.2MΩ/cm from Milli-Q is used for water droplets of 40μl in the RICM experiment. SiO_2 convex lens (f=100mm, R=51.8mm) is purchased from CASIX and used for the RICM experiment as well for the comparison. The Si substrate (Si/SiO_2) with ITO coating (30~60nm) is purchased from Sigma-Aldrich and used as a transmittable plate. The ITO coatings are also used for the electrodes of circuit to study the voltage generation experiment as well.

Table. 1. Measured radius values for the convex lens and water droplet.

	convex lens	water droplet
Radius of curvature	25.9mm	3.82mm

3.2 Experiment setup

3.2.1 Reflection Interference Contrast Microscope

A 530nm diode LED from Thorlab is used as a light source. A bottom ITO coated glass is sitting on a piezo translation stage (resolution 0.7nm, from PI E-709ERG) which controls the vertical position of *z*-direction. Reflected beam intensity is recorded by using high speed camera (PCC, v1210) with 50,000 frame/s (time interval is 20µs). An oscilloscope (from Tektronix) measures the voltage difference between the top and bottom ITOs. All system is controlled by using Labview program and synchronized. All experiments are done at the room temperature (RT) in a glove box.
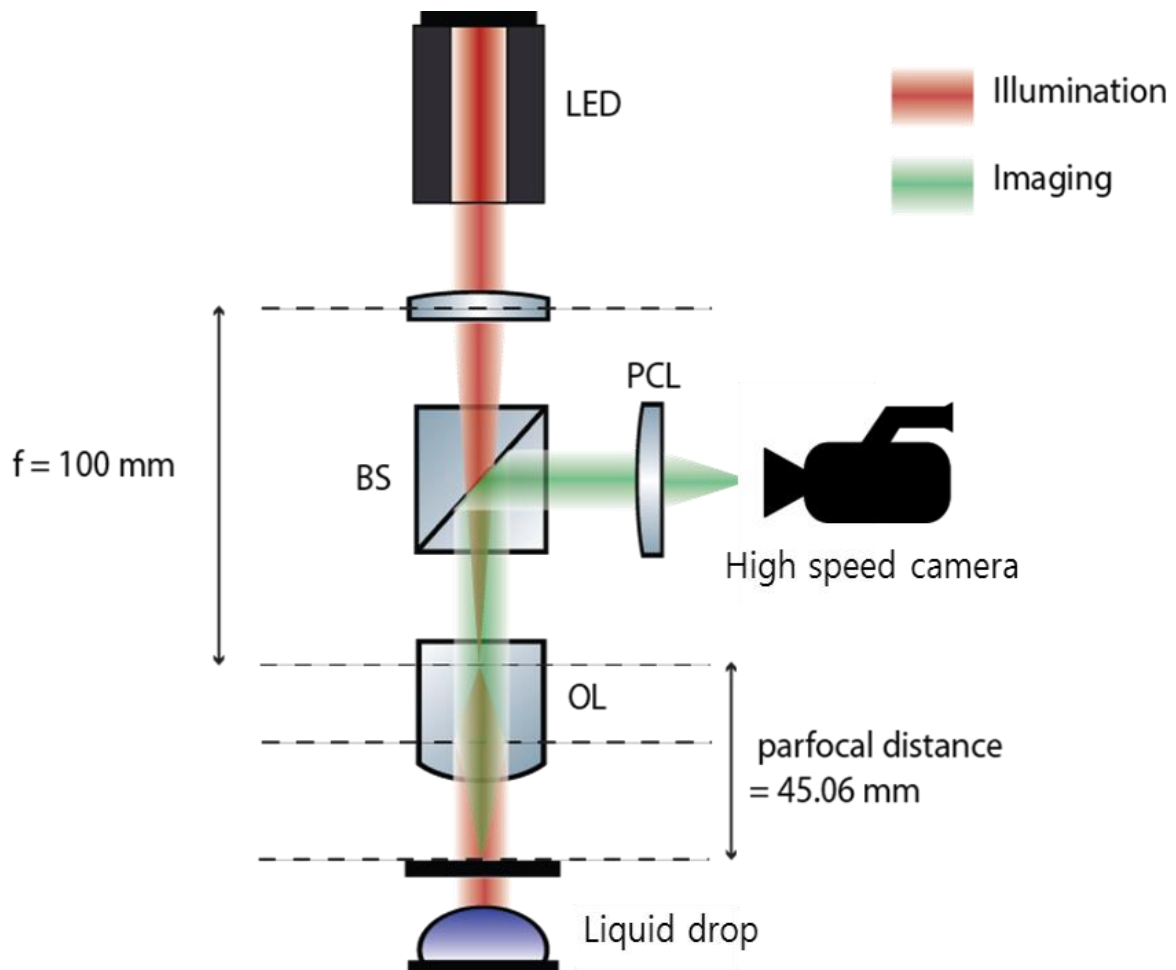

Figure 3-1. RICM for water bridge experiment.
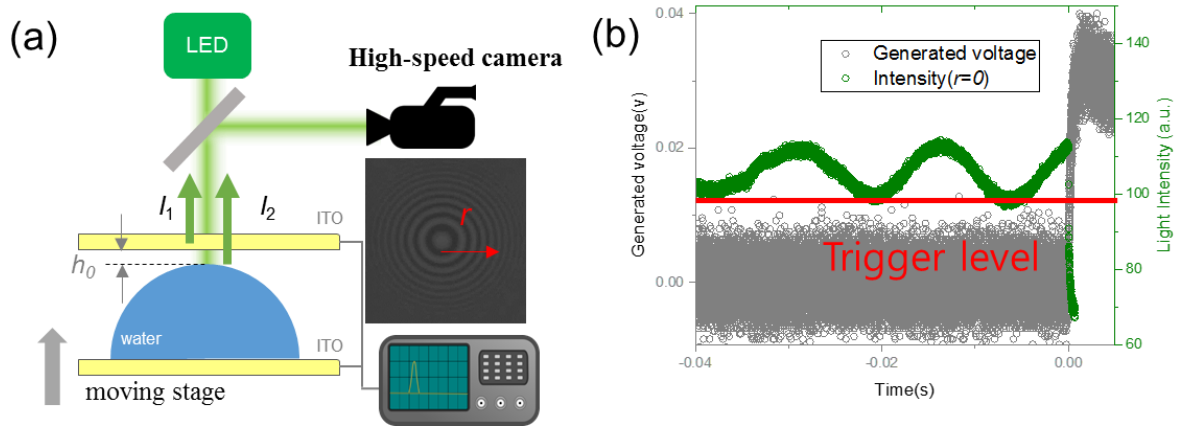
3.2.2. Voltage generation system

Figure 3-2 (a) Synchronization of two systems, the oscilloscope for the voltage generation measurement and high-speed camera for the interference image measurement. Interference image shows one real image taken by high-speed camera. (b) Synchronized data. Open gray circles and green circles represent the generated voltages and the interference light intensities, respectively. Using the trigger level of voltage (solid red line), the oscilloscope and the high-speed camera are synchronized and simultaneously start to take the data before and after the triggering point (t=0s).

Upon contact, the imbalance of charge distribution drives the charges to move from one plate to the other. And the charges in water near the top interfaces suddenly build up forming electrical double layers to balance the charge distributions of two plates. Instant voltage rise could be detected by a trigger function in oscilloscope and this triggered signal can be reference to the high-speed camera. This is the principle for the synchronization between the voltage generation and the high-speed camera. Figure 3-2 (b) shows the generated voltage with trigger level. The trigger signal selects the recording point as a reference. In this experiment, time interval of oscilloscope is ~ns and the interval of the image is 20 μs . Since the spreading radius increases with time satisfying the power-law of $r \propto t^{\alpha}$, determining the exact contact time t_0 is very important. Even very small error in determining t_0 would change the value of exponent α. We believe that our synchronization scheme gives the exact the initial contact time with 20 μs accuracy and determine the growth exponent very accurately.

3.2.3 Spreading measurement system
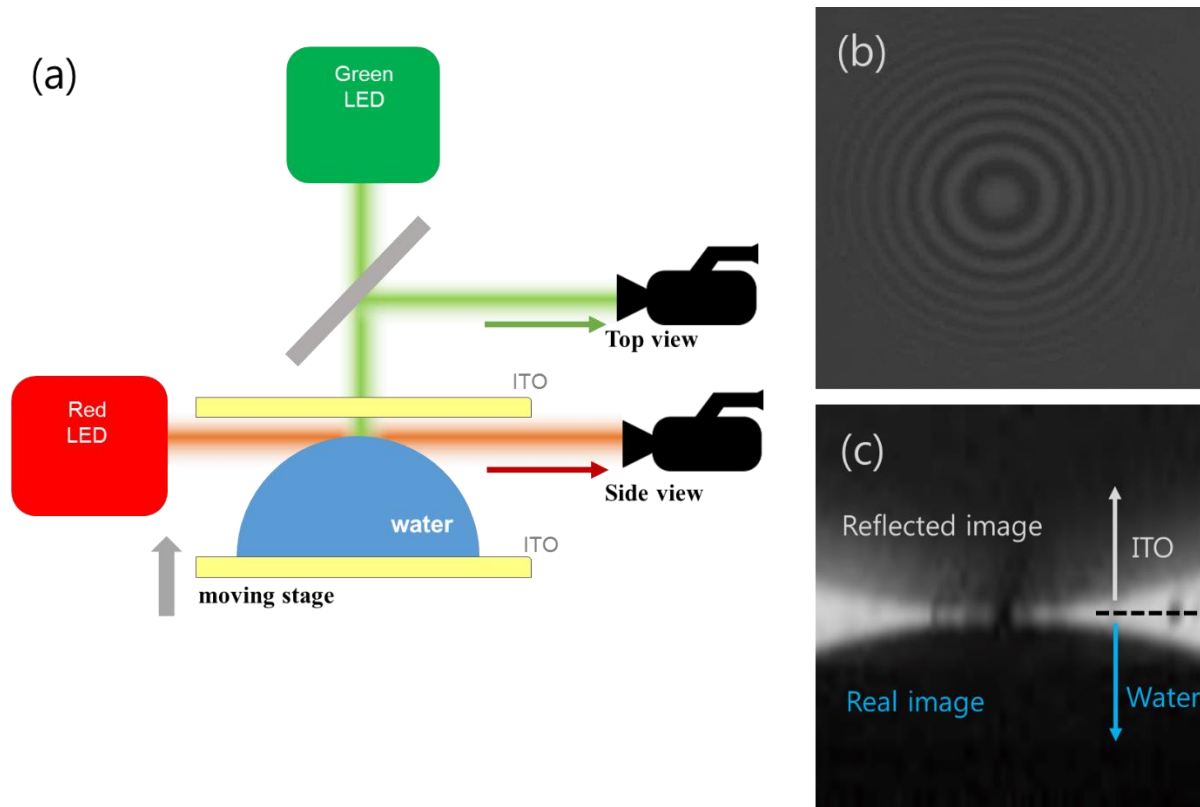
Figure 3-3 (a) Schematics of the experimental setup for the spreading measurement. Top and side views are simultaneously measured by the same high-speed camera. (b) Real image of top view. After touching, spreading interference is circular. (c) Real image of side view. Due to the reflected image, it is hard to find the exact contact time and position from the side view.

To measure the exact time of touching, two images are simultaneously captured as shown in Figure 3-3. One is the top view which shows the interference pattern, and the other is the side view which shows the real image of the droplet and the substrate. In order for this, two different diode lasers are used, green LED (λ=530nm) and red LED (λ=625nm). As shown in Figure 3-3(c), there is an artifact from the reflected image and a blurry of image due to the light diffraction caused by small gap between water droplet and top substrate making poor resolution in side view.

3.3 Interference fringe with linear motion
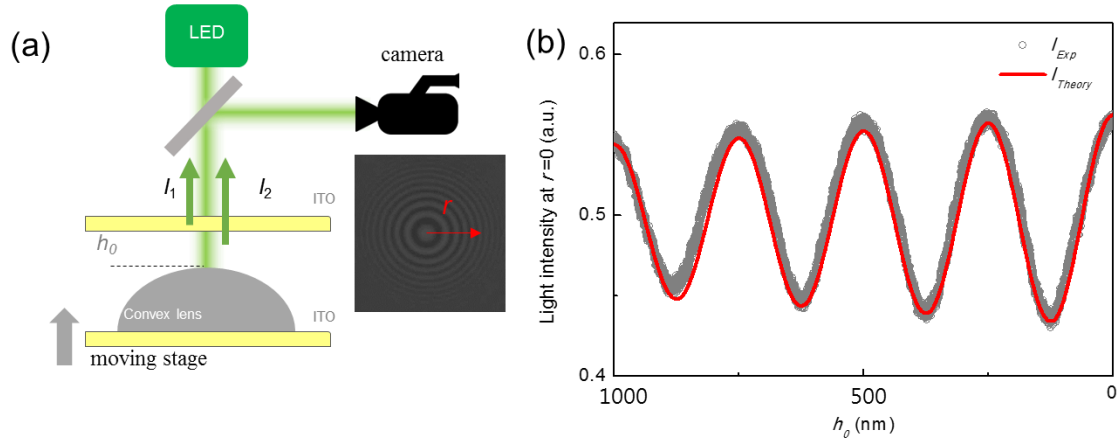
Figure 3-4 Calibration of the RICM setup (a) Schematics of RICM set up using a plano-convex lens. (b) Measured light intensity at the center of the convex lens(r=0) under continuous change of the height of sample (h_0).

To realize the high resolution observation of the touching phenomena, the resolution of translation stage is important. In this experiment, the position of the height is controlled with constant velocity (1~5 μm/s) of the piezo translation stage (resolution 0.7nm). Linear motion of the translation stage is confirmed by using a convex lens as shown in Figure 3-4. The measured data (open gray circles) agree well with the theoretical curve of Equations (2.16) and (2.17) using linear motion of convex lens ($h_o(t) = H - vt$). Here, H is the initial distance when $t = 0$.
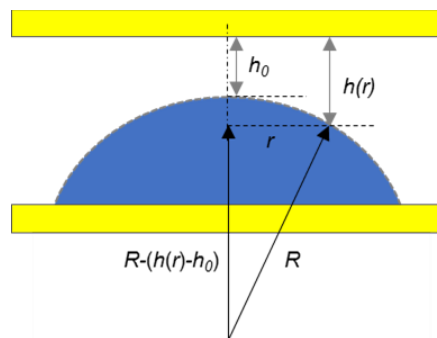
Figure 3-5. Geometrical definition in the surface morphology.

Figure 3-5 shows the geometrical definition in the surface morphology. The distance between ITO glass slide and the surface of a convex lens satisfies the following equation.

$$h(r) = h_0 + R - \sqrt{R^2 - r^2}, \tag{3-3}$$

Here, R is the radius of curvature of the convex lens used and its value is confirmed with image method also. Radius value of water droplet is also measured by image method (Table 1).

By using Equation (3.3), radial dependent height $h(r)$, and intensity interference patterns can be calculated as shown in Figure 3-6.
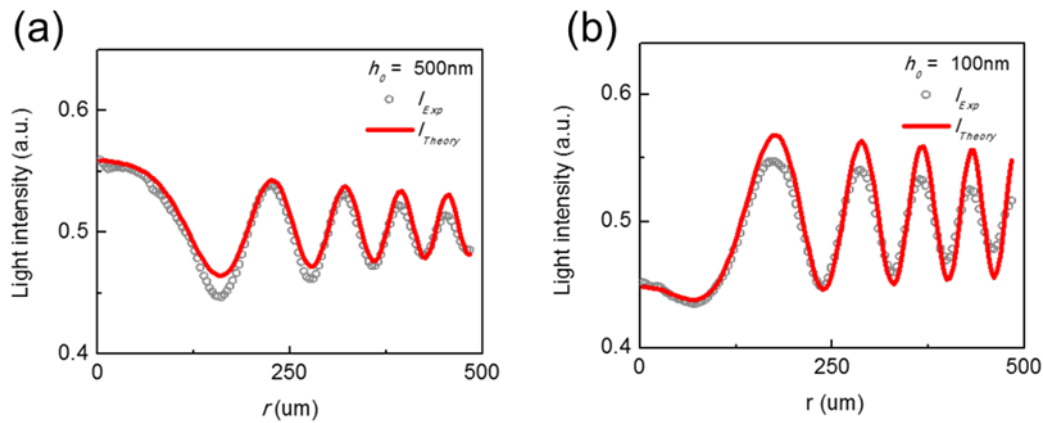
Figure 3-6. Radius dependent light intensities. (a) Measured intensities (open gray circles) and theoretical curve (solid red line) at $h_0 = 500$nm for the convex lens. (b) Measured intensities (open gray circles) and theoretical curve (solid red line) at $h_0 = 100$nm for the convex lens.

  As shown in Figure 3-6, the reflected light intensities from the convex lens for two different heights ($h_0 = 500$nm and 100nm) are well matched with the theoretical curves. As a result, the linear motion of the vertical translation stage agrees with the measured data as shown in Figures 3-4 and 3-6.

4. Result and discussion

4-1 Relation between water droplet spreading and voltage generation
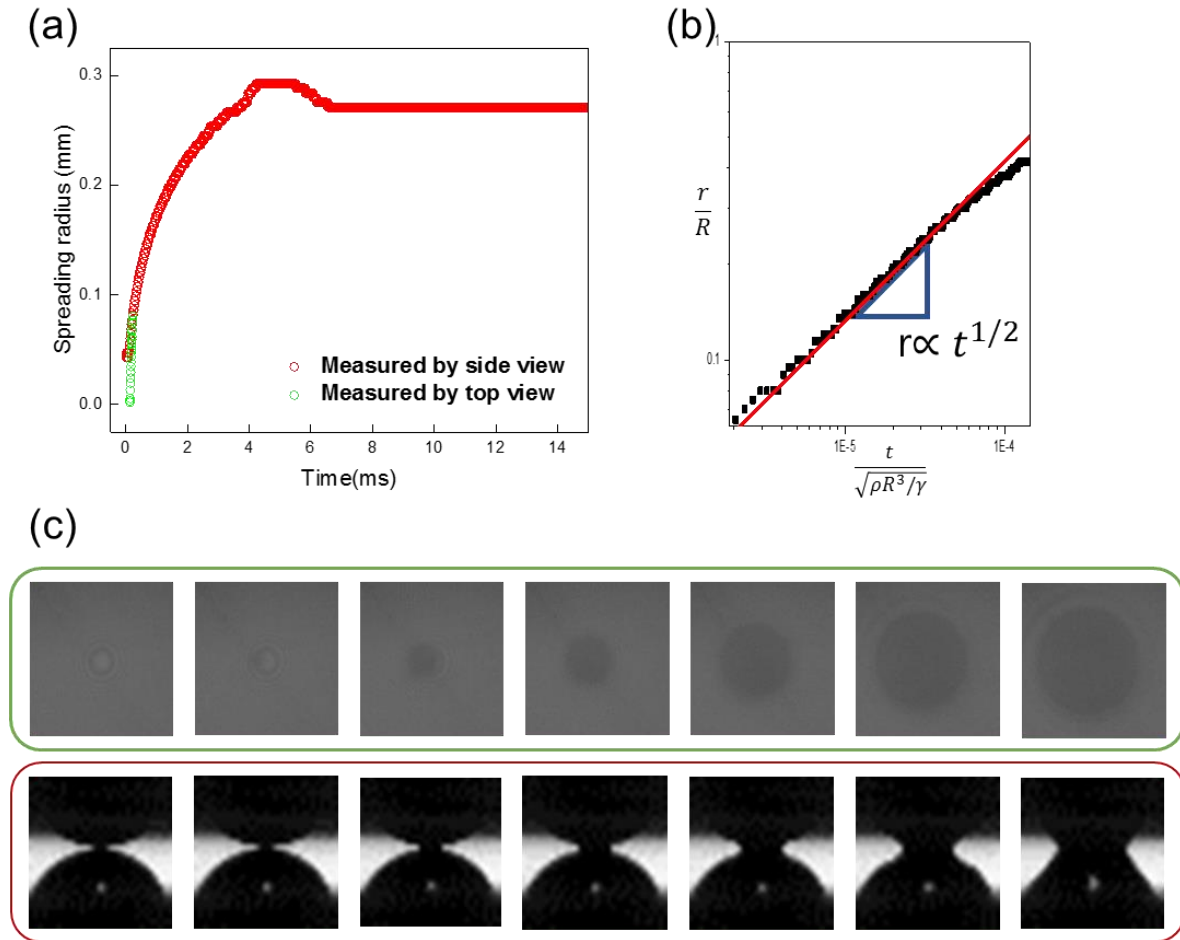
Figure 4-1. Measured spreading radius of water droplet as a function of time. (a) The red curve are data taken by side view image and open green circles are data taken by top view image. (b) Log-log plot of Figure 4-1(a). The red curve and black solid line represent the side view data and the fitted line with $t^{1/2}$. (c) The upper (inside the green square) and lower images (inside the red square) are top view and side view images, respectively. In the top view images, as the contact area is spreading after the touching, the radius of the shaded part is widening its radius with time.

According to the force balance between inertial and capillary pressure, the radius of the spreading should increase with $t^{1/2}$ according to Equation (2.4). Figure 4-1 shows the measured water droplet radius after touching ($t=0$ s). The top view image in the upper of (c) and the side view in the lower of (c) are simultaneously measured. When the spreading is monitored from a side view only, it is hard to distinguish the exact time of touching. But the top view images can clarity this. Figure 4-1 (a) and (b) show the growth of the water droplet spreading radius with time which follows the power law of $r \sim t^{1/2}$. According to Equation (2.6), the characteristic inertial time is $t_c = \sqrt{\rho R^3 / \gamma}$. Since the radius of the droplet is R=2.78mm in this experiment, the expected t_c value is about 17ms. But the power law growth ends near t =5ms, which is three times smaller than the expected. Comparison previous result with our result in figure 2-2, we can measure more short range than other result. We can measurement the spreading dynamics from 10^{-6} to few ms, but they did few ms to s order. Therefore, we can measure high short range spreading dynamics also generated voltage.

Based on the EDL theory in Equations (2.9) to (2.13), the capacitance is expected to change as the touching area changes. Figure 4-2(a) voltage generation due to spreading can be treated as the inverse process of electro wetting. Figure 4-2 (b) corresponding 0 to 6ms figure 4-2(a). Figure 4-2(c) shows the induced charge $q(t)$ calculated from the measured voltages using Equation (2.10). Here, the induced charge increases exponentially and becomes saturated within about 5 ms. Figure 4-2(d) shows the spreading radius $r(t)$ from image measurement (orange open circles) and the fitting (gray open circles) with Equation (2.13). At the time larger than 5ms, there is no change in spreading radius. The fitting agrees well with the measured data at t <5 ms. This means voltage generation is directly correlated to the water spreading effect. The spreading dynamics during the initial period less than 5ms is due to the mixed effect of the surface energy minimization and electrical energy relaxation. But the surface energy minimization seems to dominate in the early stage. The spreading radius during the time larger than 5ms is mainly from electrical energy relaxation. In this time regime, there is no change in spreading radius.
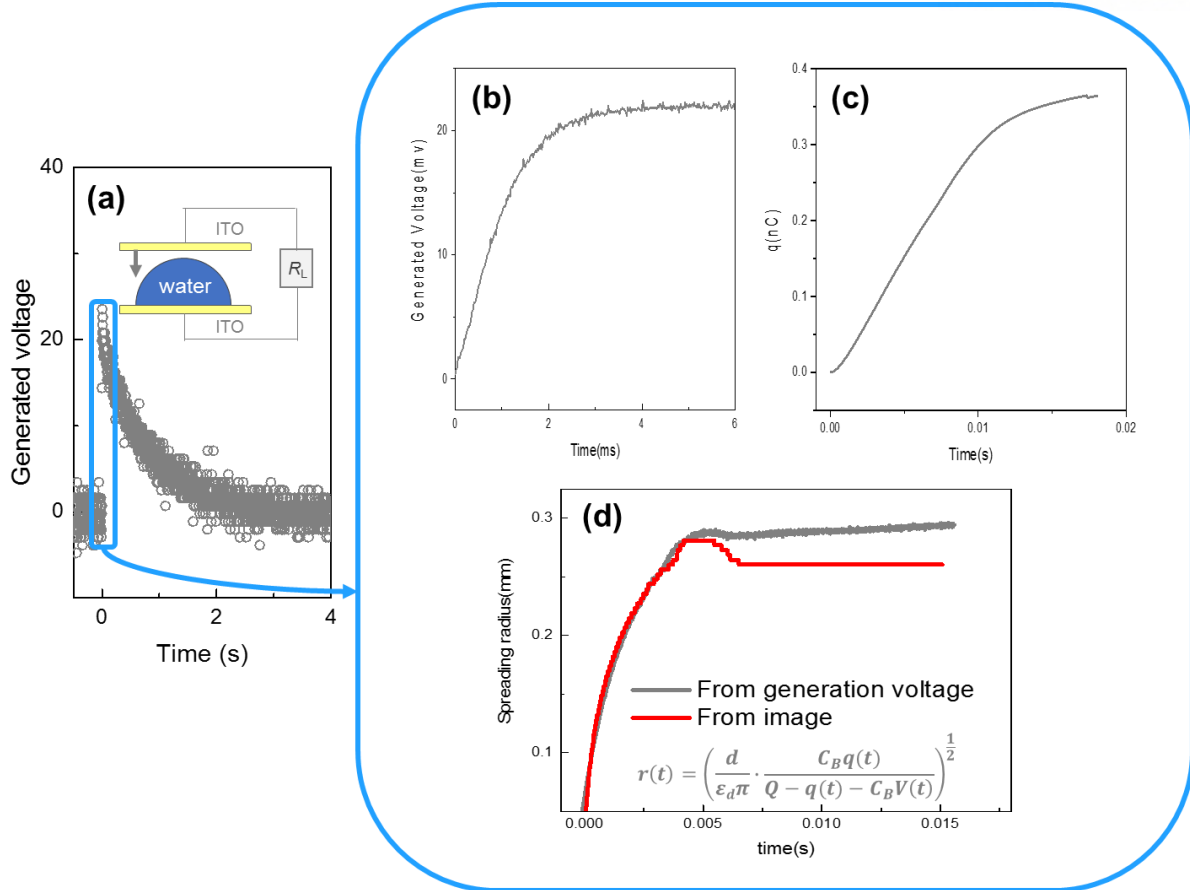
Figure 4-2 (a). Result from generated voltage between top and bottom of electrode. (b)Extended generated voltage result, from 0 to 6 ms (c). Calculated charge during water droplet spreading by using the voltage generation and the equation $q(t) = \frac{1}{R}\int V(t)dt$**. (d) Water droplet spreading radius as a function of time: the gray curve shows the calculated value from q(t) using Equation (2) and the orange one shows the direct imaging measurement.**

But the fitting parameter values of ε and d are different from the known values for bulk water and the reported values at the interface. Table 2 compares the fitting parameter values with Teschke's results. In this table, electrical permittivity ε, electrical double layer d and surface charge Q. In bulk, well-known values for these parameters are $\varepsilon = 78$ and debye length is $\sim 1\mu m$. However, near the interface according to Teschke's report, these parameters have the values of $\varepsilon = 3.8$ and $d = 60nm$.[42] He explains this difference by the water dipole reorientation at interface. Depending on solid surface structure, water molecule can reorient at solid-liquid interface. The best fitting parameter values in this experiment are $\varepsilon = 22$ (dielectric constant), d =39nm (EDL thickness), and Q=0.9nC (surface charge). .

33

We believe these values are averaged effects during the spreading. In this experiment, the water-ITO interface is not in equilibrium during the first 5 milliseconds.

Table. 2. Fitting results and reference values (at room temperature)

	ε	d	Q
For bulk water	78	~1μm (Debye length)	
For interface[42]	3.8	60nm	
In this study	22	39nm	0.9nC

4-2 Comparison between the convex lens calibration and the water droplet deformation.

Tian and Shen reported that negative ions are distributed on the water surface which has a neighbor with air[42]. When we take account the EDL formation, Coulomb interaction between solid and liquid is considerable before touching. Actually, Sacha et. al. observed a water bridge formation and explained the water bridge formation due to the Coulomb interaction with few nanometer distance between AFM tip and water surface as shown in Figure 1-1.[21-22] To observe the Coulomb interaction between ITO and water surface, we used the RICM method which has a higher distance resolution.

Figure 4-3. (a) Modulation of light intensity at the center of interference pattern (open gray circles) and theoretical curve (solid red curve) depending on the height of convex lens surfac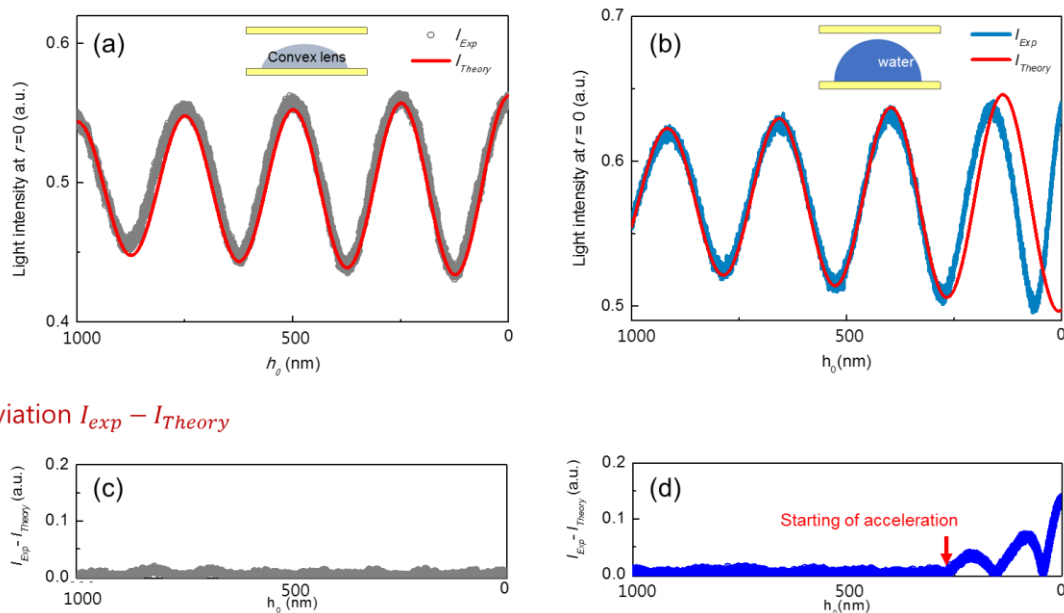e. (b) Modulation of light intensity at the center of interference pattern (open cyan circles) and theoretical curve (solid red curve) depending on the height of water droplet surface. (c) Deviation of the measured intensity from the theoretical expectation for the convex lens. (d) Deviation of the measured intensity from the theoretical expectation for the water droplet.

As a calibration, a plano-convex lens is raised with $5\mu m/s$ stage speed until it makes a contact with the top substrate. When a convex lens is used as shown in Figure 4-3(a), the interference intensity I_{exp} (r=0) at the center of the RICM interference pattern agrees with the expected value I_{Theory}, where deviation (I_{exp}-I_{Theory}) is negligibly small (see Figure 4-3(c)). In order to observe the water surface deformation, water droplet is raised to the top substrate with the same speed as shown in Figure. 4-3(b). But when a water droplet is used, the interference intensity I_{exp} (r=0) at the center of the RICM interference pattern starts deviating from the expected value I_{Theory} for undeformed water droplet at the specific height. It means that there is some change in the water droplet surface curvature starting from the specific height. Deviation (I_{exp}-I_{Theory}) is too large to ignore. The faster oscillation of curve means the faster approaching of water droplet than speed of stage. From the starting point of deviation shown in Figure 4-3(d), we define the starting point of acceleration of water surface. Interestingly, starting of acceleration is 273nm, and this value is very different from the previously reported value of ~5nm [21,22].
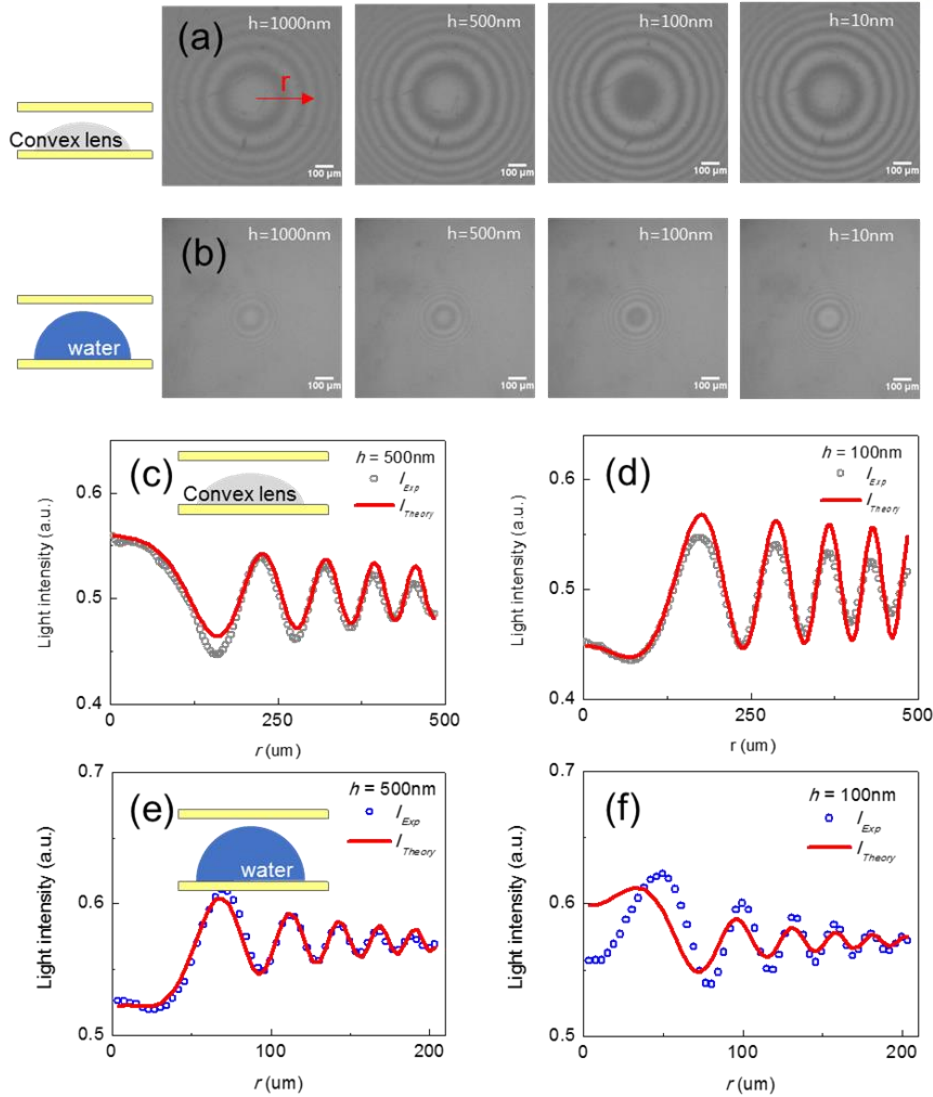
Figure 4-4. Interference light intensity as a function of radial distance from the symmetric center in RICM interference pattern. (a), (b) Fringe patterns at 4 different heights for convex lens (a), and for water droplet (b). (c) Modulation of light intensities (open gray circles) and theoretical curve (solid red curve) at h_0 = 500nm for the convex lens. (d) Modulation of light intensities (open gray circles) and theoretical curve (solid red curve) at h_0 = 100nm for the convex lens. (e) Modulation of light intensities (open blue circles) and theoretical curve (solid red curve) at h_0 = 500nm for the water droplet. (f) Modulation of light intensities (open blue circles) and theoretical curve (solid red curve) at h_0 = 100nm for the water droplet.

Water has a high surface tension. If there is an acceleration of the center position (r=0), therefore, radius dependent height changes should be considerable as well. Figures 4-4(a), and (b) show the camera images at certain positions, and Figures 4-4(c)-(f) show the circular averaged fringe patterns for both of convex lens (gray circles) and water droplet (blue circles). Theoretical curves (red curves) are

based on the height changes due to the surface curvature. Open blue circles in Figures 4-4(e) and (f) show the interference intensity I_{exp} of the RICM interference pattern as a function of the radial distance from the symmetric center. When a convex lens is used, the interference intensity I_{exp} (open gray circles) agrees with the expected value I_{Theory} (red solid curve). But when a water droplet is used, the interference intensity I_{exp} starts deviating from the expected value I_{Theory} at specific distance. In (a), water droplet surface data agrees with the theoretical value at $h_0 = 500nm$. But in (b) at $h_0 = 100nm$, there is large mismatch between the measurement and theoretical expectation and deviation amounts are reduced by increasing the radius. When we take account the distance change due to the surface curvature, reduced deviation is reasonable.

4-3 Deformation of the water droplet surface by long range interaction

Modulation of interference intensity occurs due to the phase difference between to the two reflected lights as in Equations (2.16) and (2.17), which are the result of the optical path length difference. When there is no deformation of the droplet surface in time, the interference intensity should follow Equation (2.16). But, as we can see the data for $h_0=100nm$, there is a discrepancy between I_{Exp} and I_{Teory}. This can be fixed by adjusting the distance $h_0(t)$ between the water surface and ITO substrate by replacing $h_0(t)$ to $h_0(t) - \Delta d(t)$. Here, $\Delta d(t)$ is called as deformation length, and we can replace Equation (2.16) with the following equation,

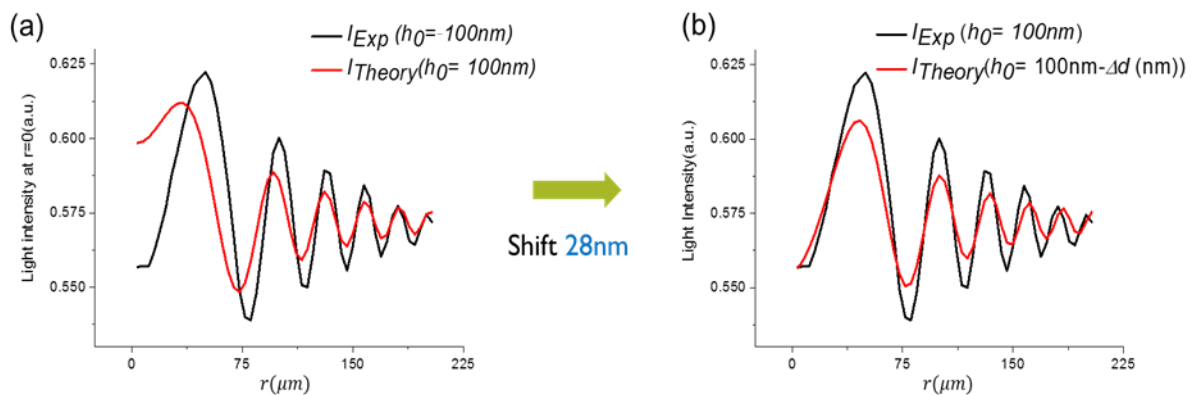$$I(h(r)) = I_1 + I_2 + 2\sqrt{I_1 I_2} \cos\emptyset(h_0(t) - \Delta d(t)) \qquad (4.2)$$

Figure 4-5 Disagreement between I_{Exp} of water and I_{Theory} at h_0=100nm can be fixed by adjusting the distance h_0 to h_0-Δd at h_0=100nm. Here, $\Delta d = 28$nm.

Figure 4-6(a) is the interference intensity I_{Exp} and I_{Teory} for water at h_0 =100nm showing the discrepancy between the measurement and the theory. According to Figure 4-4(d), the deviation starts at h_0=273nm. Therefore, in order to match the data with the theory, we replaced the $h_0(t)$ with $h_0(t) - \Delta d(t)$. In Figure 4-5(b), the measurement agrees with the theory well by shifting the curve with 28nm (=Δd).
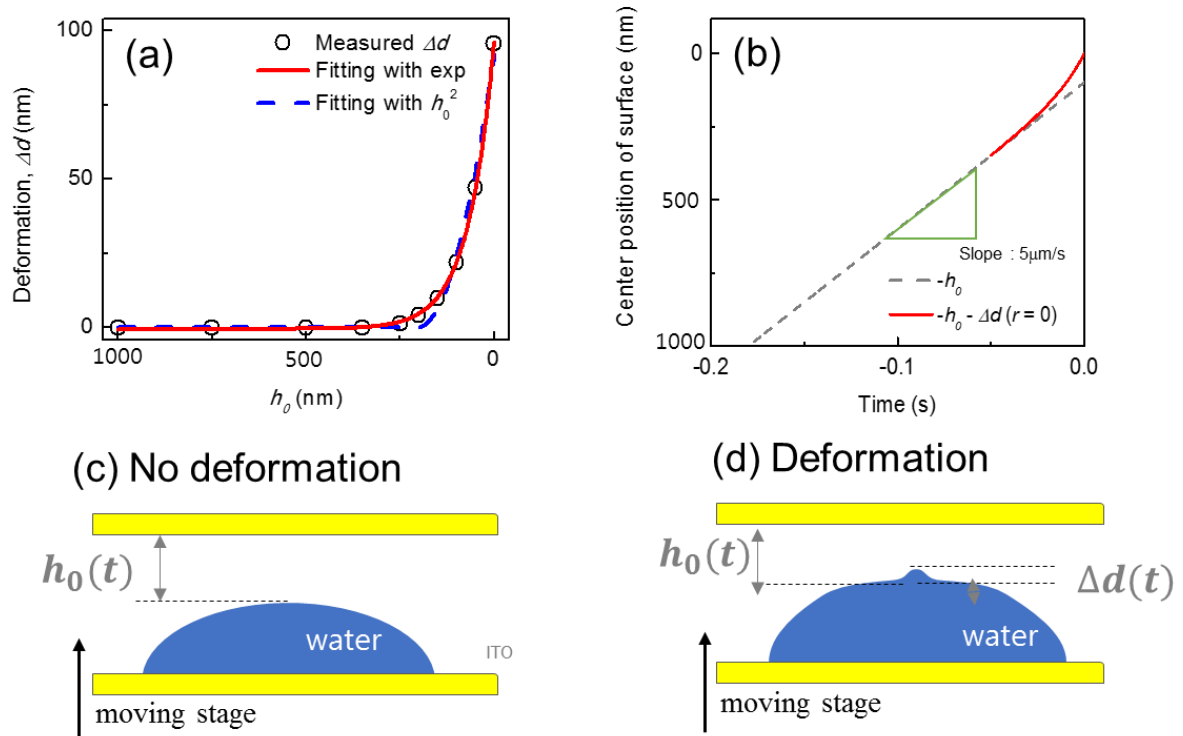

Figure 4-6. (a) Measured deformation length (open black circles) depending on the distance h_0. Solid red curve and dashed blue curve represent the fitting curves with single exponential and with degree 2 polynomial, respectively. (b) Time dependent value of the top position of the droplet surface. Dashed gray line represents the top position of the droplet without deformation, only due to the linear motion of an upwardly moving translation stage. The solid red curve is the measured position due to acceleration. Therefore, the deviation length corresponds to the deformation amount of the droplet surface. (c) and (d) represent two different surface geometries, respectively, without deformation (c) and with deformation (d).

Using the same method, we can calculate the deformation length from the symmetric center r=0 to r=200μm and plot the surface deformation morphology. Interestingly, deformation amounts are well matched with the exponential fitting (solid red curve) than 2nd order polynomial fitting (dashed blue curve). This may be due to faster acceleration with stronger Coulomb interaction.
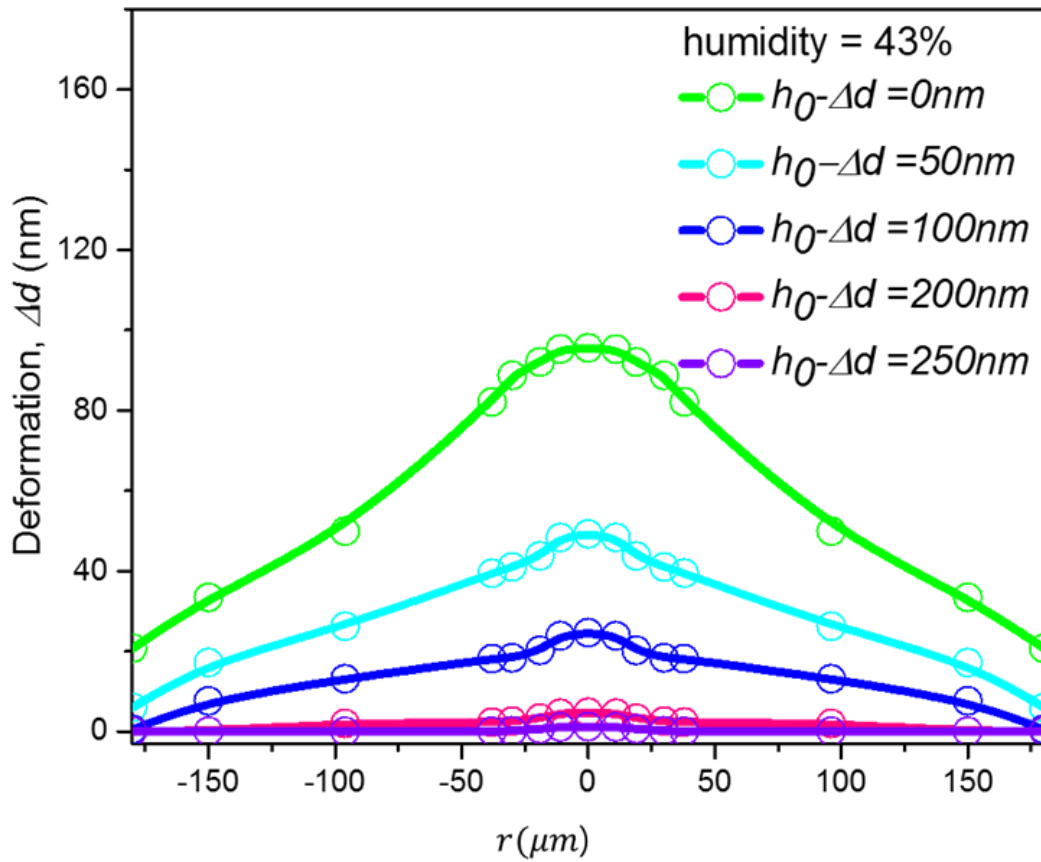
Figure 4-7 Water droplet surface deformation morphology depending on radius dependent deformation amount (Δd) at five different water droplet positions (h_0).

From the interference intensity and Equation (4.2), we can obtain the surface deformation morphology by using the measured distance between the water droplet and the top ITO substrate. Figure 4-7 shows the radius dependent deformation amounts at different positions (h_0) of water droplet. As shown in this figure, deformation amount is higher at the center part of water surface. Several possibilities are remained as the origin of this behavior. (1) faster condensation (2) localized charges, (3) faster acceleration. Related with these questions, we need also to consider the water evaporation of and non-equilibrium deformation morphology of the system.

4.4 Non-equilibrium dynamics of surface deformation

Figure 4-8 shows the deformation amounts depending on h_0 for 3 different stage speeds (from 1 to 5μm/s). Here, the slower stage moving speed, the larger deformation. If this observation is from the evaporation effect, it should show opposite result. This means that the surface relaxation is slower than the moving speed of the translation stage, and the measured results don't represent the true equilibrium deformation depending on the vertical distance. But, if we decrease the stage speed further, the evaporation effect will dominate the surface morphology.
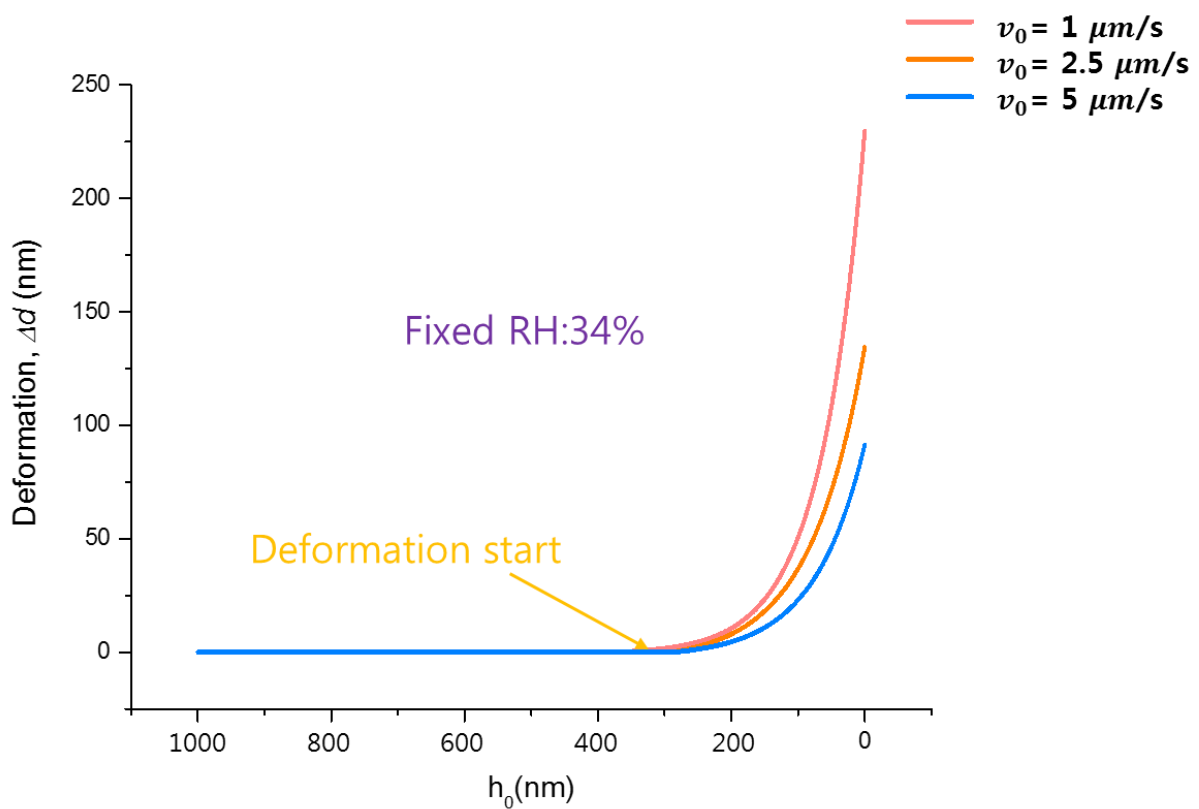

Figure 4-8 Water surface deformation for three different stage speeds

4-5 Competition between deformation and evaporation

To observe the surface deformation due to evaporation, the deformation is measured at different relative humidity conditions with the stage speed of 1 μm/s.
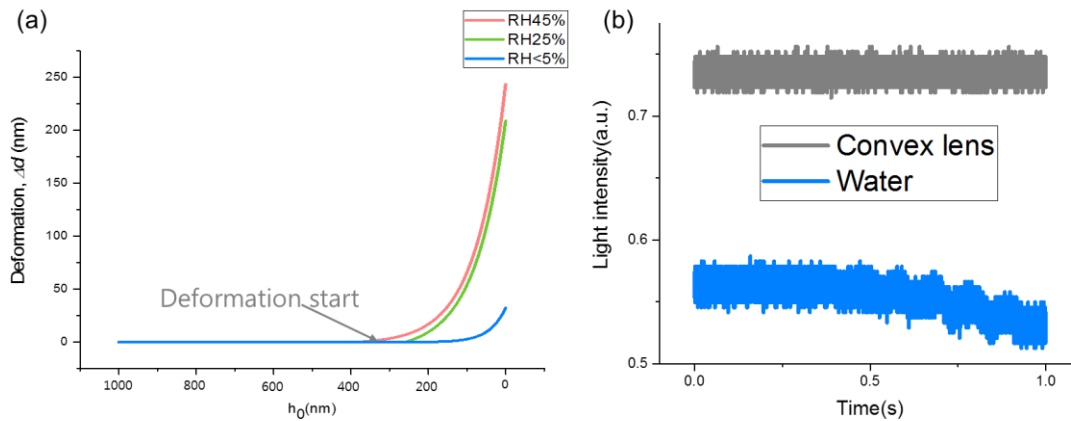

Figure 4-9 Evaporation effect with different relative humidity conditions. (a) Water droplet deformation for three different relative humidity conditions (RH = 45%, 25%, <5%). Stage speed is fixed at 1μm/s. (b) Light intensity changes at the fixed position of r=0 for RH<5%. Solid gray and blue curves represent the intensity changes for convex lens and for water droplet, respectively.

As shown in Figure 4-9 (a), the deformation amount shows a negligible humidity dependency at high relative humidity condition (RH > 25%). But the deformation decreases a lot at low humidity condition. This means that the faster evaporation at low humidity decreases the deformation effect. To confirm the evaporation, the interference intensity change with time is measured for a convex lens and a water droplet at the fixed position. Figure 4-10 (b) shows the RICM light intensities at the symmetric center at fixed vertical distance for RH<5%. When a convex lens is used, the intensity does not change with time. But when a water droplet is used, the intensity decreases with time. These two data mean that there is huge effect of evaporation for low relative humidity. Therefore, only the experiments at higher relative humidity (>25%) can be reliable.
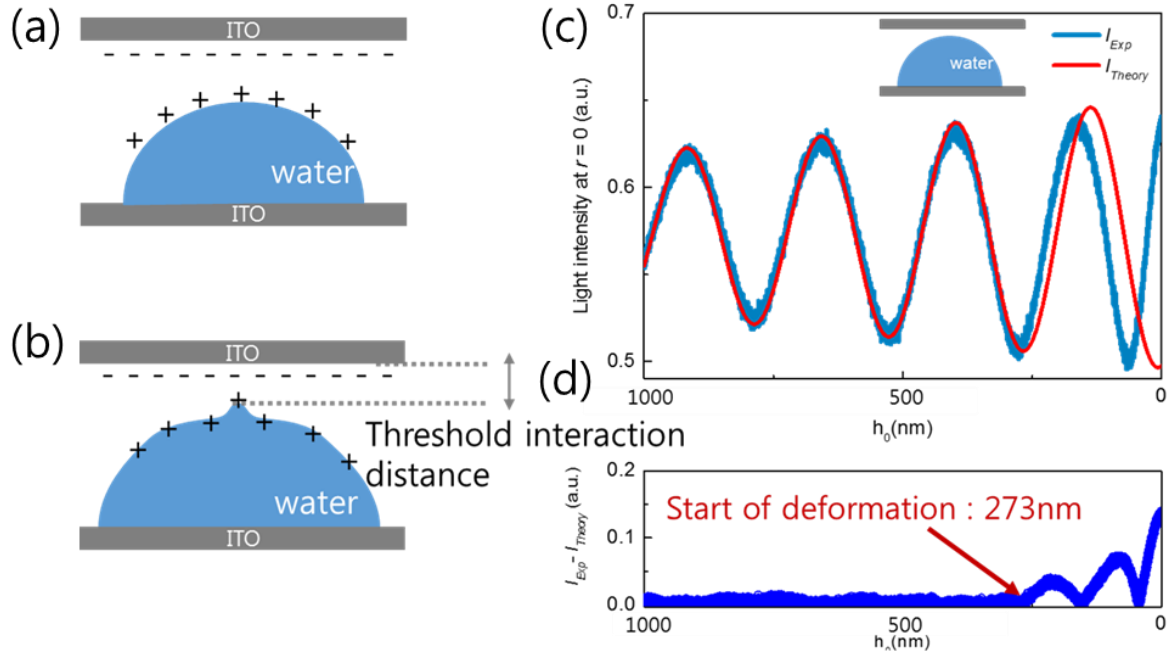
4.6 Physical origin for surface deformation

Figure 4-10 Possible origin of water surface deformation due to spontaneous charge accumulation. (a) No deformation of water surface when the distance is far. (b) Water surface deformation due to the electrostatic attraction between the positively charged water surface and the negative image charges in metal surface. (c) and (d) show the water surface deformation depending on distance from solid surface.

Figure 4-10 shows the possible origin for the water surface deformation near metal surface. It has been known that water surface is weakly negatively charged and the bare metal surface does not have surface charge. But as two surfaces are approaching each other, in order to lower the total free energy, the water surface becomes positively charged. Because of this, there are negative image charges in the metal. Therefore, there is an electrostatic attractive force between water surface and the metal surface. When the distance is far, the attractive force is not big enough and there is no deformation on water surface as in (a). But, when the distance is enough, the large attractive force deforms the top edge of the water droplet as in (b).

Since the typical distance forming the water bridge in this work is much larger than the characteristic distance of ~5nm in the previously reported work in which the water bridge forms due to the water vapor condensation and the externally applied electric field, we believe that water surface deformation at long range is due to Coulomb interaction.

43

5. Conclusion

Despite of its importance, solid-liquid interface is not well understood yet. To investigate the solid-liquid interface we build up a home-made experimental system: combination of voltage generation system and RICM. Using this, we studied two important properties of the solid-liquid interface: spreading dynamics of water droplet on metal surface and the surface deformation of water droplet near the substrate before contact.

To understand the water droplet spreading dynamics, the spreading radius and the voltage generation are simultaneously measured. The spreading radius grows with time following the power law of $r \sim t^{1/2}$. The power law growth ends near t =5ms, which is three times smaller than the expected characteristic inertial time of $t_c = \sqrt{\rho R^3 / \gamma} = 17$ms.

Based on the electrical double layer capacitor (EDLC) model, we found a strong correlation between the generated voltage and the spreading radius. The best fitting parameter values to the correlation are $\varepsilon =$ 22 (dielectric constant), d =39nm (EDL thickness), and Q=0.9nC (surface charge). Smaller values of dielectric constant and charge interaction length had been suggested by several theoretical and experimental studies. But, we believe these values are averaged effects during the spreading. In this experiment, the water-ITO interface is not in equilibrium during the first several milliseconds.

In order to study the surface deformation due to the interaction between the solid and liquid surfaces before the contact, the RICM system with nano-meter resolution is used. When a plano-convex lens (hard hemisphere) is approached to the ITO surface, the observed interference patterns agree well with the expected linear motion of the lens surface. But, when a water droplet surface is used instead, there is a deformation in the droplet surface without any externally applied electric field. Interestingly, the deformation starts at the distance of 300nm from the ITO surface. Droplet surface morphology is obtained from the radius dependent deformation at given distance. The surface morphology shows the formation of water bridge depending on the distance between the solid and the liquid surfaces. Even though maximum amount of observed deformation is ~100nm, all the observed morphology seems to show only the non-equilibrium surface states. Additional experimental results of humidity and stage speed dependencies suggest that the deformation larger than 250nm is expected in the equilibrium condition. This result suggests that the origin of large deformation in this experiment is completely different from the previously reported work in which the water bridge forms at the distance of ~5nm. [22]

. REFERENCE

1. B. Kang, G. Ceder, *"Battery materials for ultrafast charging and discharging"*, Nature 2009, 458, 190-193.

2. L. L. Zhang, X. S. Zhao, *"Carbon-based materials as supercapacitor electrodes"*, Chem. Soc. Rev. 2009, 38, 2520-2531.

3. F. Boulmedais, C. S. Tang, B. Keller, J. Vörös, *"Controlled Electrodissolution of Polyelectrolyte Multilayers: A Platform Technology Towards the Surface-Initiated Delivery of Drugs"*, Adv. Funct. Mater. 2006, 16, 63-70.

4. M. A. Brusatori, Y. Tie, P. R. Van Tassel, *"Protein Adsorption Kinetics under an Applied Electric Field: An Optical Waveguide Lightmode Spectroscopy Study"*, Langmuir 2003, 19, 5089-5097.

5. M. A. Shannon, P. W. Bohn, M. Elimelech, J. G. Georgiadis, B. J. Marias, A. M. Mayes, *"Science and technology for water purification in the coming decades"*, Nature 2008, 452, 301-310.

6. R. Zhao, P. M. Biesheuvel, H. Miedema, H. Bruning, A. van der Wal, *"Charge efficiency: A Functional Tool to Probe the Double-Layer Structure Inside of Porous Electrodes and Application in the Modeling of Capacitive Deionization"*, J. Phys. Chem. Lett. 2010, 1, 205-210.

7. R. A. Hayes, B. J. Feenstra, *"Video-speed electronic paper based on electrowetting"*, Nature 2003, 425, 383-385.

8. R. B. H. Veenhuis, E. J. van der Wouden, J. W. van Nieuwkasteele, A. van den Berg, J. C. T. Eijkel, *"Field-effect based attomole titrations in nanoconfinement"*, Lab Chip. 2009, 9, 3472-3480.

9. M. S. Kilic, M. Z. Bazant, A. Ajdari, *"Steric effects in the dynamics of electrolytes at large applied voltages. I. Double-layer charging"*, Phys. Rev. E 2007, 75, 021502.

10. P. Bruesch, T. Christen, *"The electric double layer at a metal electrode in pure water"*, J. Appl. Phys. 2004, 95, 2846-2856.

11. M. Mezger, H. Schroeder, H. Reichert, S. Schramm, J. S. Okasinski, S. Schoeder, V. Honkimaeki, M. Deutsch, B. M. Ocko, J. Ralston, M. Rohwerder, M. Stratmann, H. Dosch, *"Molecular Layering of Fluorinated Ionic Liquids at a Charged Sapphire <0001> Surface"*, Science 2008, 322, 424-428.

12. A. Uysal, H. Zhou, G. Feng, S. S. Lee, S. Li, P. Fenter, P. T. Cummings, P. F. Fulvio, S. Dai, J. K. McDonough, Y. Gogotsi, *"Structural origins of Potential Dependent Hysteresis at the Electrified Graphene/Ionic Liquid Interface"*, J. Phys. Chem. C 2014, 118, 569-574.

13. M. A. Gebbie, H. A. Dobbs, M. Valtiner, J. N. Israelachvili, *"Long-range electrostatic screening in ionic liquids"* PNAS 2015, 112, 7432-7437.

14. A. M. Smith, A. A. Lee, S. Perkin, *"The Electrostatic Screening Length in Concentrated Electrolytes Increases with Concentration"* J. Phys. Chem. Lett. 2016, 7, 2157-2163.

15. C. S. Tian, Y. R. Shen, *"Structure and charging of hydrophobic material/water interfaces studied by phase-sensitive sum-frequency vibrational spectroscopy"*, PNAS 2009, 106, 15148-15153.

16. S. C. Flores, J. Kherb, N. Konelick, X. Chen, P. S. Cremer, *"The Effects of Hofmeister Cations at Negatively Charged Hydrophilic Surfaces"*, J. Phys. Chem. C 2012, 116, 5730-5734.

17. J. Huang, A. Malek, J. Zhang, M. H. Eikerling, *"Non-monotonic Surface Charging Behavior of Platinium: A Paradigm Change"*, J. Phys. Chem. C 2016, 120, 13587-13595.

18. J. K. Moon, J. J, J. L, H. K. Pak*, "Electrical power generation by mechanically modulating electrical double layers"*, Nat. Commun. 2013, 4, 1487.

19. J. K. Moon, M. W. Song, H. K. Pak, *"Investigation of surface charge density on solid-liquid interfaces by modulating the electrical double layer"*, J. Phys.: Condens. Matter 2015, 27, 194102.

20. M. Z. Bazant, B. D. Storey, A. A. Kornyshev, *"Double Layer in Ionic Liquids: Overscreening versus Crowding"*, Phys. Rev. Lett. 2011, 106, 046102.

21. G. M. Sacha, J. J. Saenz, C. Montserrat, G. Ricardo, *"Field-Induced Formation of Nanometer-Sized Water Bridges"*, Phys. Rev. Lett. 2003, 91, 056101.

22. G. M. Sacha, A. Verdaguer, M. Salmeron, *"Induced Water Condensation and Bridge Formation by Electric Fields in Atomic Force Microscopy"*, J. Phys. Chem. B 2006, 110, 14870-14873.

23. A. Eddi, K. G. Winkels, J. H. Snoeijer, *"Short time dynamics of viscous drop spreading"*, Phys. Fluids 2013, 25, 013102.

24. B. B. J. Stapelbroek, H. P. Jansen, E. S. Kooij, J. H. Snoeijer, A. Eddi, *"Universal spreading of water drops on complex surfaces"*, Soft Matter, 2014, 10, 2641-2648.

25. G. Verma, M. Pandey, K. P. Singh, *"Interferometric technique for nanoscale dynamics of fluid drops on arbitrary substrates"*, J. Appl. Phys. 2015, 118, 035306.

26. L. Tanner, *"The spreading of silicone oil drops on horizontal surfaces"*, J. Phys. D: Appl. Phys. 12, 1–14 (1979).

27. Winkels, K. G. *"Fast contact line motion: fundamentals and applications,"* [Online]. Available: http://doc.utwente.nl/84200. (2013)

28. J. C. Bird, S. Mandre, and H. A. Stone, *"Short-time dynamics of partial wetting"*, Phys. Rev. Lett. 100, 234501 (2008).

29. Jacco H. Snoeijer and Bruno Andreotti *"Moving Contact Lines: Scales, Regimes, and Dynamical Transitions",* Annual review of fluid mechanics 45 269-292 (2013).

30. Reto B. Schoch, Jongyoon Han, and Philippe Renaud, *"Transport phenomena in nanofluidics"*, 2008 Rev. Mod. Phys. 80 839.

31. Bazant M Z, Thornton K and Ajdari A,*" Diffuse-charge dynamics in electrochemical systems "*, 2004 *Phys. Rev.* E 70 021506

32. Klarman D, Andelman D and Urbakh M,*" A Model of Electrowetting, Reversed Electrowetting, and Contact Angle Saturation "*, 2011 *Langmuir* 27 6031–41

36. Jun Araki,*" Electrostatic or steric? – preparations and characterizations of well-dispersed systems containing rod-like nanowhiskers of crystalline polysaccharides"* Soft Matter, 2013, 9, 4125

37. Laurent Pilon, Hainan Wang, and Anna d'Entremont, *Journal of The Electrochemical Society*, 162 (5) A5158-A5178 (2015)

38. R. Kotz and M. Carlen, *Electrochimica Acta*, 45(15), 2483 (2000).

39. Jose C. Contreras-Naranjo, James A. Silas, and Victor M. Ugaz, *"Reflection interference contrast microscopy of arbitrary convex surfaces"*, 2010 Optical Society of America

40. Limozin L, Sengupta K. *"Quantitative Reflection Interference Contrast Microscopy (RICM) in Soft Matter and Cell Adhesion"*2009, Chemphyschem, 10,2752-2768.

41. Jose C. Contreras-Naranjo & Victor M. Ugaz,"*A nanometre-scale resolution interference-based probe of interfacial phenomena between microscopic objects and surfaces*" Nature Communications 4, 1919

42. O. Teschke, G. Ceotto, and E. F. de Souza *"Interfacial water dielectric-permittivity-profile measurements using atomic force microscopy "*, Phys. Rev. E 64, 011605 (2001)

Acknowledgement